Observing the disintegration of the A68A iceberg from space

A. Braakmann-Folgmann [a],[*], A. Shepherd [a], L. Gerrish [b], J. Izzard [a], A. Ridout [c]

[a] Centre for Polar Observation and Modelling (CPOM), University of Leeds, Leeds LS2 9JT, UK
[b] British Antarctic Survey, Cambridge CB3 0ET, UK
[c] Centre for Polar Observation and Modelling (CPOM), University College London, London, UK

ARTICLE INFO

ABSTRACT

Icebergs impact the physical and biological properties of the ocean where they drift, depending on the degree of melting. We use satellite imagery and altimetry to quantify the area, thickness, and volume change of the massive A68A iceberg from its calving off the Larsen-C Ice Shelf in July 2017 until January 2021, when it disintegrated. A68A thinned from 235 ± 9 to 168 ± 10 m, on average, and lost 802 ± 34 Gt of ice in 3.5 years, 254 ± 17 Gt of which was through basal melting (a lower bound for the immediate fresh water input into the ocean). Basal melting peaked at 7.2 ± 2.3 m/month in the Northern Scotia Sea and an estimated 152 ± 61 Gt of freshwater was released off South Georgia, potentially altering the local ocean properties, plankton occurrence and conditions for predators.

1. Introduction

Icebergs impact and interact with the Antarctic environment through a range of processes. This begins with their calving, which may influence the stability of their parent ice shelf (Rott et al., 1996) and flow of glaciers upstream (Rignot et al., 2004). As they drift, icebergs release cold fresh melt water, altering the local ocean properties (Helly et al., 2011; Jenkins, 1999) and facilitating sea ice growth (Bintanja et al., 2015; Merino et al., 2016). They also carry debris with terrigenous nutrients, which supply the majority of iron input to the Southern Ocean (Wu and Hou, 2017), fostering biological production (Biddle et al., 2015; Duprat et al., 2016; Smith et al., 2007). When icebergs ground, they impact marine benthic communities (Barnes, 2017; Gutt, 2001) and leave plough marks on the sea floor (Wise et al., 2017). Furthermore, large icebergs can act as a barrier disrupting the local ocean circulation (Grosfeld et al., 2001) or blocking access of penguin colonies to their feeding grounds (Kooyman et al., 2007). The response of icebergs to the warmer climates they drift through can also inform predictions on how the Antarctic ice shelves will react to climate change (Scambos et al., 2008; Shepherd et al., 2019).

A68A was the sixth largest iceberg ever recorded in satellite observations (Budge and Long, 2018), and had a significant potential to

impact its environment. Indeed when it calved from the Larsen-C Ice Shelf in July 2017, concerns were raised that its loss might trigger a collapse of the entire ice shelf (Hogg and Gudmundsson, 2017; Jansen et al., 2015). After residing close to its calving position for over a year, A68A started to move northwards through the Weddell Sea (Fig. 1). It reached the Scotia Sea in early 2020 and approached South Georgia at the end of 2020, where it started to disintegrate. Although this is a common trajectory for icebergs (Fig. 1 and Tournadre et al., 2016), the sheer size of A68A elevates its potential to impact ecosystems around South Georgia through release of fresh water and nutrients, through blockage and through collision with the benthic habitat (Grimm, 2021; Vernet et al., 2012). Here, we combine satellite imagery and satellite altimetry to chart changes in the A68A iceberg's area, freeboard, thickness, volume and mass over its lifetime to assess its disintegration and melt rate in different environments.

2. Data and methods

We track the iceberg's area and area change in satellite imagery. In total, 23 Sentinel-1, 18 Moderate Resolution Imaging Spectroradiometer (MODIS) and 14 Sentinel-3 scenes are used to manually delineate the iceberg's outlines using GIS software. While the Sentinel-1 Synthetic

Aperture Radar (SAR) imagery offers all-weather capability and higher spatial resolution, MODIS and Sentinel-3 optical imagery have the advantage of a higher temporal resolution, but cannot be used during the polar night and on cloudy days. In optical imagery the spatial resolution is slightly lower and it is harder to distinguish sea ice from icebergs or clouds, which is the main error source. Therefore, we rely on Sentinel-1 data, if available close to the altimetry overpasses and use MODIS or Sentinel-3 data on the other occasions. To estimate the accuracy of our delineations we buffer the polygon outlines by two pixels and calculate the resulting difference in area. This gives a mean relative difference of 3.2%.

Changes in the iceberg's freeboard and thickness are derived from CryoSat-2 and ICESat-2 satellite altimetry. To generate a complete map of the initial iceberg freeboard and thickness, we collect all CryoSat-2 tracks over the part of the Larsen-C Ice Shelf that formed the A68A iceberg between 12 July 2016 and 11 July 2017 (Fig. 2), correcting for the mean ice motion of 696 m/year (Mouginot et al., 2019). To track changes in the iceberg freeboard while it is drifting, we colocate 15 overpasses from ICESat-2 and 9 overpasses from CryoSat-2 with the initial freeboard map, post them on a common 2-km grid, and difference them. For this colocation to the initial iceberg reference system, we digitize the iceberg outline in a near-coincident image using 7 Sentinel-1 and 17 MODIS scenes. We then transform this outline to maximize the overlapping area with respect to the outline of the previous overpass. At least for icebergs like A68A that are non-symmetric and when the general shape is preserved, this step-wise transformation yields the optimal rotation and translation parameters defining where the new overpass

samples the iceberg and which part of the initial freeboard map this corresponds to (Fig. 3). Grid cells of the initial map that are not covered by any track are filled using linear interpolation.

The CryoSat-2 data are processed from Level 1B baseline D using the Centre for Polar Observation and Modelling sea ice processing system (Tilling et al., 2018). For consistency, a common threshold retracker is applied to measurements acquired in both SAR and SAR interferometric mode and over all surface types. Iceberg freeboard is calculated by subtracting the adjacent mean sea surface height from the iceberg surface height. For ICESat-2 we use Level 2A, ATL03 photon data as a primary product, because iceberg heights are filtered out in the higher level products. For each track, we analyze the three strong beams separately and discard the weak beams. Low confidence flagged photons (2 and below) are filtered out and 150 photons each are averaged along-track, to reduce noise. We then extract the mean sea surface height, ocean tides and inverted barometer effect from Level 3A version 3 ATL07 data, interpolated to the ATL03 locations. These are subtracted from the photon heights, yielding sea surface heights that agree with the ATL07 sea surface heights, and to derive iceberg freeboard. Finally, we discard freeboard measurements from both altimeters below 20 and above 100 m and measurements outside the iceberg polygon derived from the near-coincident satellite imagery. To make the higher resolution ICESat-2 data comparable to the initial heights derived from CryoSat-2, we also filter out crevasses searching for local minima with a prominence of 3 or more and reject the outer 2 km at the edges.

Uncertainty estimates are a combination of the freeboard standard deviations and the impact of the colocation uncertainty. The colocation
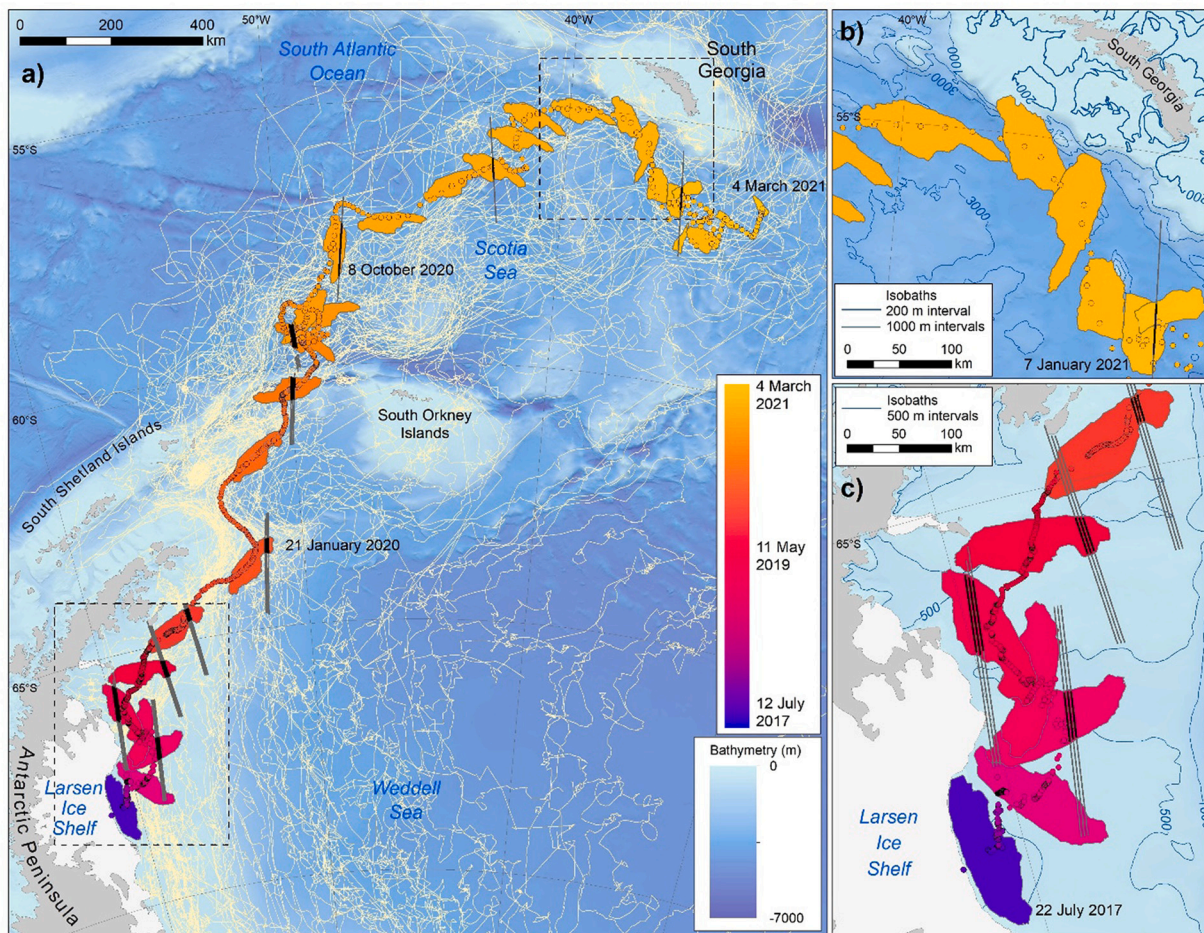
Fig. 1. Trajectory of A68A (circles colored by date) and historic icebergs (yellow lines, Budge and Long, 2018) overlain on a bathymetric map (GEBCO Compilation Group, 2019; Hogg et al., 2016). Selected outlines (date colour coded), altimetry overpasses (grey lines with black marking the parts that sample the iceberg) and key dates are also shown. Panels b and c are zoom regions of interest.
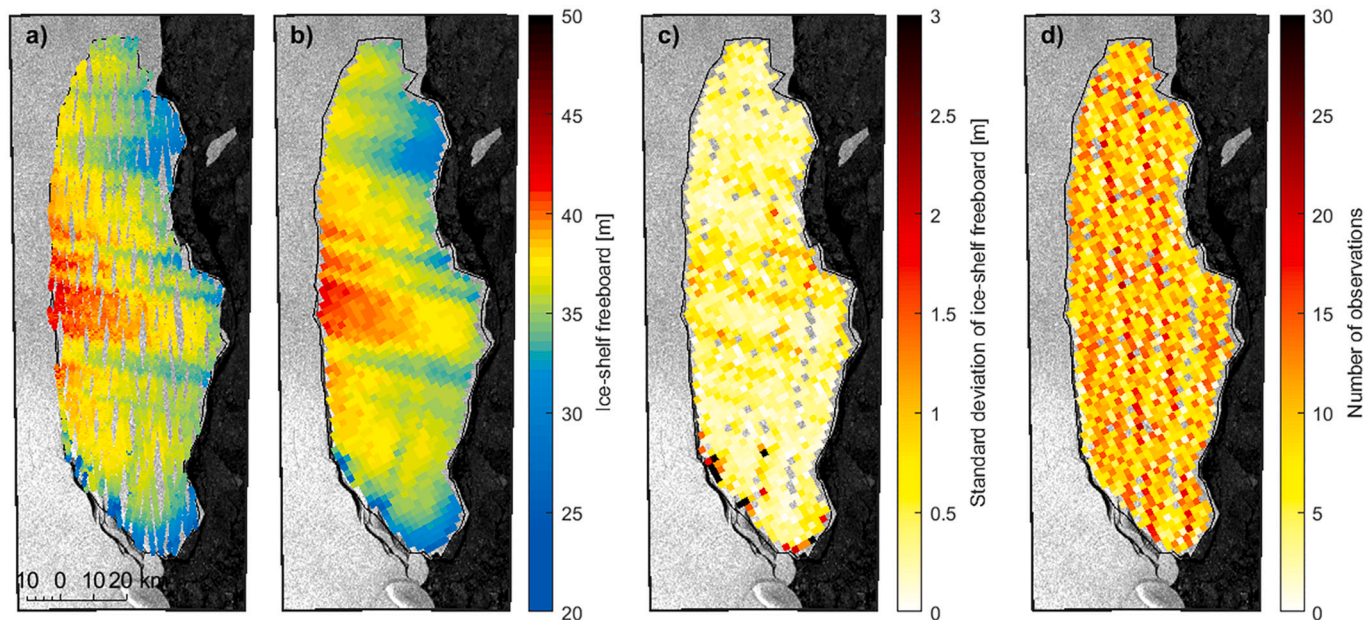
Fig. 2. Calculation of initial iceberg freeboard map: (a) CryoSat tracks over the Larsen-C Ice Shelf over 1 year (12 July 2016–11 July 2017) before the iceberg calved, cut to the area that later formed the iceberg. (b) The same measurements gridded at 2 km and empty grid cells filled with linear interpolation. (c) Standard deviation within each grid cell. (d) Number of observations averaged per grid cell. The background shows a Sentinel-1 image on 10 July 2017.
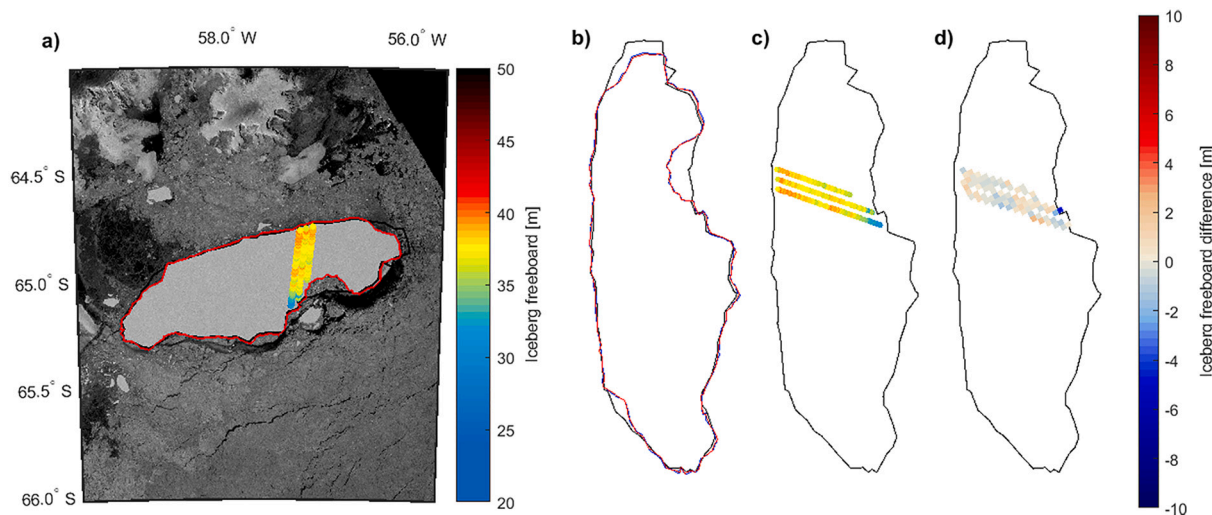

Fig. 3. Colocation of a sample ICESat-2 track and the corresponding Sentinel-1 image on 18 September 2019: For each altimetry overpass a near-coincident image is used to derive the iceberg's outline at the time of the new overpass (red, panel a). The new outline is transformed to maximize the overlapping area with the previous outline (blue, panel b). This is done iteratively, so we know the transformation of the previous polygon with respect to the initial polygon (black) and can transform the new overpass to the initial situation (panel c). We then grid the new track on the same grid as the initial freeboard measurements and difference it with these initial heights (panel d).

uncertainty is mainly caused by the time separation between the altimetry overpass and the corresponding image. We perform a Monte Carlo simulation using 1000 samples that are normally distributed around the estimated translation and rotation assuming a maximum (3 sigma) daily rotation of 15 degrees and a maximum translation based on the drift speed of the iceberg scaled by the time separation. The drift speed is calculated as the path distance (Greene et al., 2017) from the locations given in the Antarctic Iceberg Tracking database (Budge and Long, 2018). We then calculate the freeboard difference for each of the 1000 slightly differently colocated samples and take their standard deviation as an estimate of the impact of erroneous colocation. This colocation uncertainty is combined with the standard deviations of the initial freeboard and of the new overpass using uncertainty propagation.

The freeboard standard deviations are calculated within each grid cell. When the whole track is averaged to derive the mean freeboard change at one point in time, the uncertainties of the involved grid cells are propagated. Rather than assume that our freeboard measurement errors are not correlated in space or time, we employ a more conservative approach and propagate the uncertainties using a full covariance matrix to account for their correlation (Storto et al., 2019). In the absence of independent freeboard measurements for verification, we assume that altimeter-derived freeboards recorded along the same track are 60% correlated and that the initial freeboards, which are derived from measurements acquired along several independent tracks, are 30% correlated. The mean standard deviation of the calculated freeboard change is 0.45 m, with colocation contributing 22%, the initial

freeboard contributing 29% and the new track contributing 49%.

Iceberg thickness H is derived from iceberg freeboard h_{fb} assuming hydrostatic equilibrium (Eq. 1). We treat ICESat-2 and CryoSat-2 measurements in the same way, presuming neither penetrates the snow layer. Because the iceberg survives for several years and travels a long distance passing through varying environmental conditions, we model the evolution of the snow layer and iceberg density based on ERA5 Reanalysis data (Copernicus Climate Change Service, 2018) of air temperature, wind speed and snow accumulation (Fig. 4, Braakmann-Folgmann et al., 2021). The iceberg's column-average density ρ_i reduces from 868 to 848 kg m^{-3} during its drift (Ligtenberg et al., 2011), because the densest, pure glacial ice is melted from the bottom. We estimate the uncertainty in the column average and basal ice densities to be 10 kg m^{-3} (Dryak and Enderlin, 2020) and 2 kg m^{-3}, respectively. The density of the surface snow layer ρ_s reaches 465 kg m^{-3} after 3.5 years (International Organization for Standardization, 1998) and snow depth h_s increases by 3.3 m. We estimate the snow density and depth uncertainties to be 50 kg m^{-3} (Kurtz and Markus, 2012) and 20% (Kwok and Cunningham, 2008), respectively. As sea water density ρ_w we use 1024 kg m^{-3} (Fichefet and Morales Maqueda, 1999) with an uncertainty of 2 kg m^{-3}. Altogether, the mean uncertainty in thickness change is 5.3 m, with ice density uncertainty being the largest factor. To obtain a continuous representation of iceberg thickness in space and time, we fit a third order polynomial function of latitude, longitude and time to our observations of thickness change and combine this with the initial thickness map (supplementary animation, Braakmann-Folgmann et al., 2022).

$$H = \frac{\rho_w}{\rho_w - \rho_i} h_{fb} - \frac{(\rho_w - \rho_s)}{\rho_w - \rho_i} h_s \qquad (1)$$

Iceberg volume is determined by multiplying iceberg thickness and area, interpolated to the times of the altimetry overpasses. Changes in the volume of the mother iceberg are then calculated by differencing each volume estimate to the initial value. We differentiate between volume loss through fragmentation (area loss) and volume loss through basal melting (thickness change) by keeping either thickness or area constant. To convert volume change to mass change, we multiply the loss due to fragmentation by the column-average ice density at each point in time, and we multiply the basal thickness change by the density of pure glacial ice. Summing both components gives the total iceberg mass change. Uncertainties are propagated, and we find that the uncertainties in area and thickness change contribute 45% and 55%, respectively, to the uncertainty of volume change.

3. Results

The initial area of the A68A iceberg was 5719 ± 77 km^2. Since A68A and A68B separated just after calving (Budge and Long, 2018, Fig. 5a), our initial polygon shows the outline of the A68A iceberg and all our results relate to A68A. During its lifetime, the iceberg's area gradually reduced both through larger break-ups and continuous processes (Figs. 1 and 6a). A larger break-up took place between 2018 and 2019 and another large piece, A68C, was lost in April 2020. In December 2020, the A68A iceberg gave birth to several children icebergs, named A68D-A68F (Budge and Long, 2018), rapidly reducing the area of the remaining largest part. Apart from these sudden losses, iceberg area also reduced gradually through side melting and smaller edge-wastings. Overall, the iceberg lost 3206 ± 78 km^2 up to 7 January 2021, when our last thickness measurement is, and 5052 ± 106 km^2 by 4 March 2021 - a $56 \pm 8\%$ and $88 \pm 4\%$ reduction in area of the mother iceberg, respectively. We find distinct patterns of area change according to the iceberg's geographical location (Fig. 6a), with a mean loss rate of 200 ± 82 km^2 per year in the Weddell Sea and a more than ten times higher loss rate of 2807 ± 199 km^2 per year in the Scotia Sea until 7 January 2021, when the iceberg is drifting in open ocean.

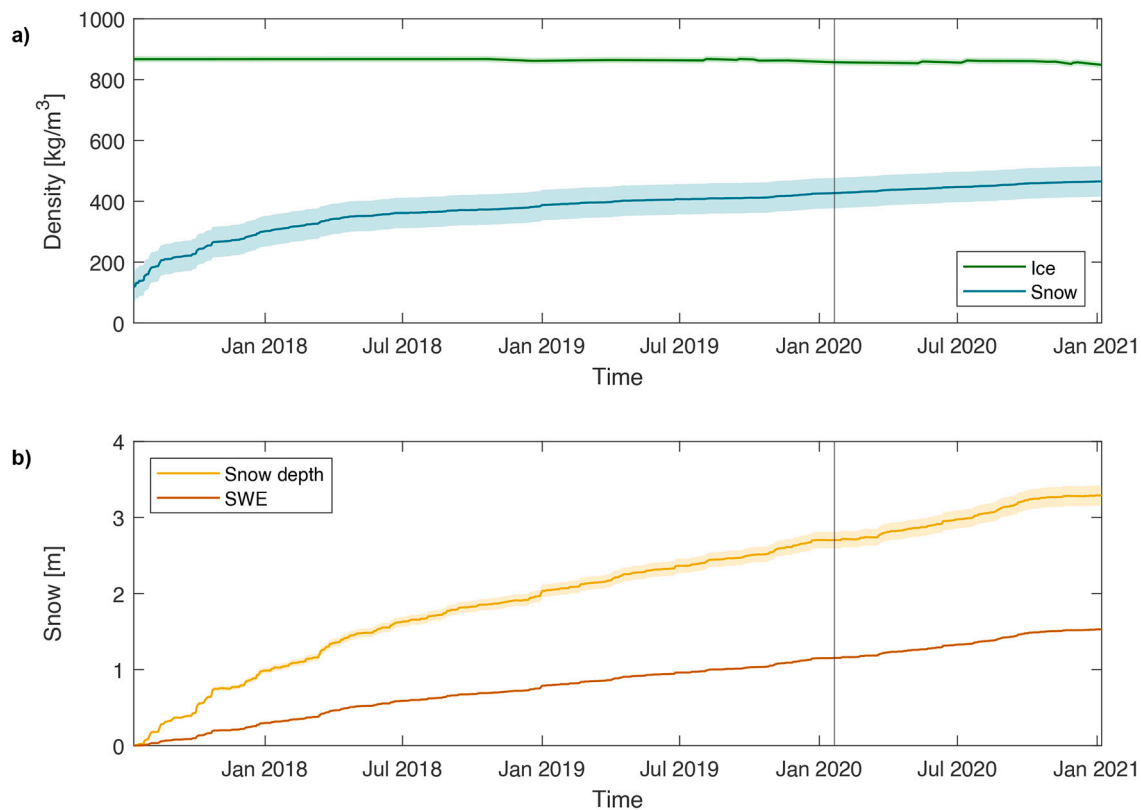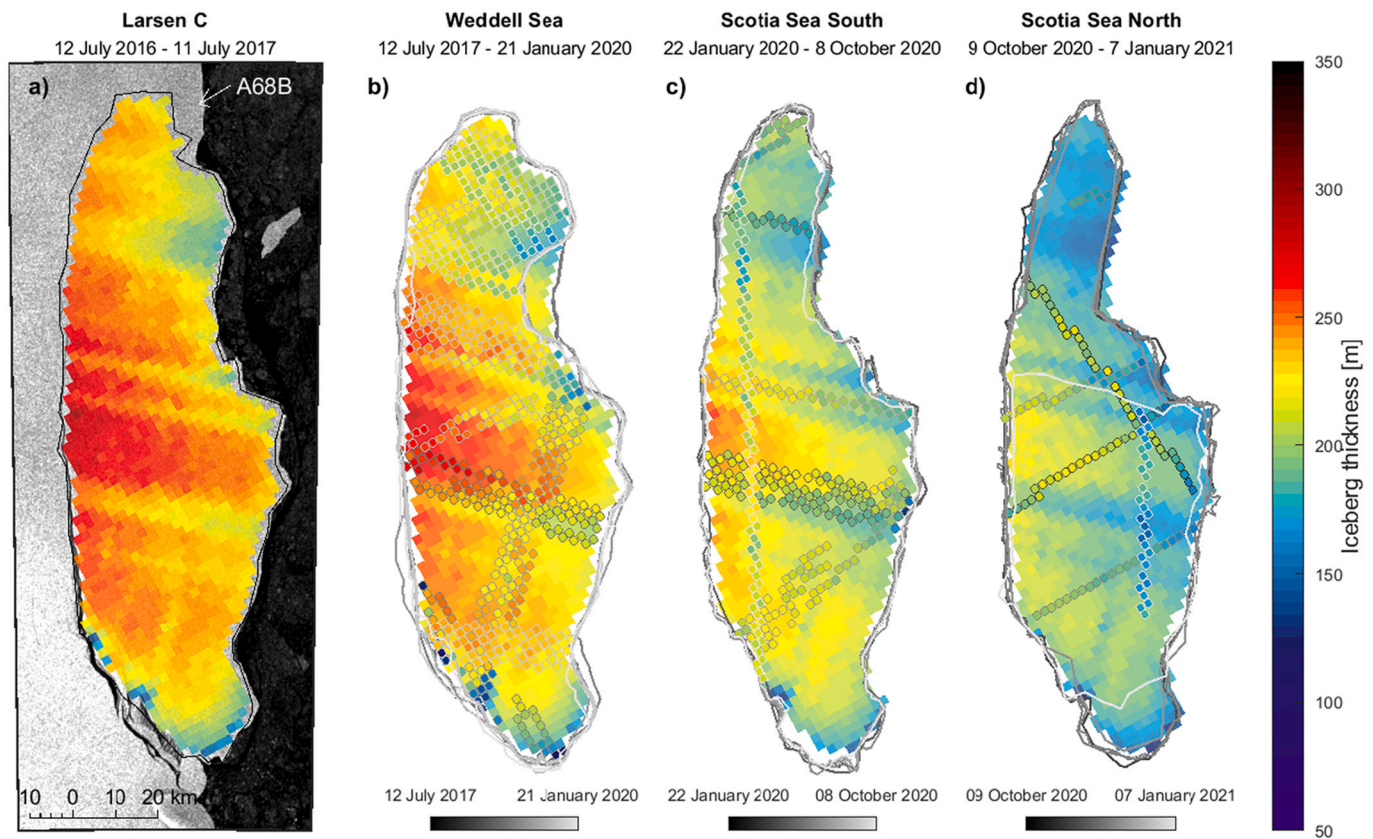The maps of initial iceberg freeboard and thickness (Figs. 2 and 5a)

Fig. 4. Evolution of iceberg properties based on ERA-5 Reanalysis data (Copernicus Climate Change Service, 2018): (a) Iceberg density and snow density; (b) snow depth and snow water equivalent (SWE).

Fig. 5. Maps of the A68A iceberg thickness when it was still part of the Larsen-C Ice Shelf (a) and at later dates as it drifted through the Weddell and Scotia Seas (b-d). The initial thickness is superimposed on a Sentinel-1 image acquired on 10 July 2017, and the region from which A68B was formed is also indicated. On later dates, the iceberg thickness is computed at colocated altimetry overpasses (outlined gridcells, shaded according to date relative to the interval start) and modelled at the mid-point of each interval elsewhere.

reveal the iceberg's topography. The mean gridded initial freeboard is 36.0 ± 0.2 m and the mean estimated initial iceberg thickness is 235 ± 9 m. The iceberg was thicker on the side facing the Antarctic Peninsula and thinnest on the Southern tip, where the crack which separated the iceberg from the ice shelf started (Jansen et al., 2015), and in the North. Moreover, the iceberg is covered by longitudinal surface structures in the former ice shelf flow direction of a few meters depth, which extend across the iceberg's full width and are a few kilometers wide, widening towards the sea. These are not visible in optical or radar imagery, but revealed by the thickness. One of these features coincides with a suture zone (Jansen et al., 2013). Owing to the undulating topography, gridded freeboard heights range from 22.1 to 42.6 m, and this motivates our colocation of subsequent altimetry tracks to improve confidence in estimates of freeboard and thickness change.

The iceberg freeboard stays almost constant while in the Weddell Sea with a mean freeboard loss of 0.2 ± 0.1 m/year (Fig. 6b), but starts to rapidly decrease once it enters the Scotia Sea, where the mean rate of freeboard lowering is 5.7 ± 0.4 m/year. Marking the location of each track, we observe that the initially southern part of the iceberg is the most resilient to melting. This explains the positive outliers in the time series, which all stem from the southern part. For thickness change (Figs. 5, 6c and supplementary animation) we record a total reduction of 67 ± 5 m, leaving the iceberg with a mean thickness of 168 ± 10 m close to South Georgia. The mean melt rates are 7.8 ± 2.1 m/year in the Weddell Sea and 49.5 ± 6.5 m/year in the Scotia Sea (3.0 ± 0.8 m/ month in the Southern and 7.2 ± 2.3 m/month in the Northern Scotia Sea). We find good agreement (average RMSE 10 m, maximum RMSE 22 m) between our observed iceberg thickness and the model fit (Fig. 5). Another finding from our study is that CryoSat-2 and ICESat-2 freeboard and thickness measurements over the iceberg are comparable and can be merged into a consistent time series (see Fig. 6b, c - especially the tracks on 5 and 16 May 2020, which are close in time).

The A68A iceberg's initial volume was 1346 ± 53 km^3. After 3.5 years, the volume of the mother iceberg had reduced by 924 ± 27 km^3 (Fig. 6d), which is $69 \pm 3\%$ of its initial value. Converted to mass loss this corresponds to 802 ± 34 Gt lost from the mother iceberg. Fragmentation makes up for $68 \pm 5\%$ of the total mass loss and basal melting accounts for the remaining $32 \pm 3\%$. While both processes contribute roughly equally in the Weddell Sea and increase as the iceberg drifts northwards, fragmentation becomes the dominant wastage factor as the iceberg falls apart and forms numerous children icebergs in the Northern Scotia Sea (Fig. 6d, Table 1). The total loss through basal melting (277 ± 19 km^3 or 254 ± 17 Gt) can be considered as a lower estimate of the immediate freshwater flux along the iceberg's trajectory. However, smaller edge wastings will add to this and also larger children icebergs will eventually melt, but not necessarily at the location where they are lost.

4. Discussion

Our findings compare well with previous studies of the Larsen-C Ice Shelf and of icebergs that followed similar trajectories. For example, our initial iceberg density of 868 kg m^{-3} is consistent with the estimated ~15 m firn air content derived from airborne observations (Holland et al., 2011) and our estimates and spatial distribution of initial iceberg thickness and freeboard agree very well with iceberg drafts derived from the same airborne campaign (Holland et al., 2009) and from in situ measurements collected along the suture zone (Jansen et al., 2013). Lopez-Lopez et al. (2021) estimated the area of A68A between 22 July 2017 and 26 January 2019 using a largely automated approach, and
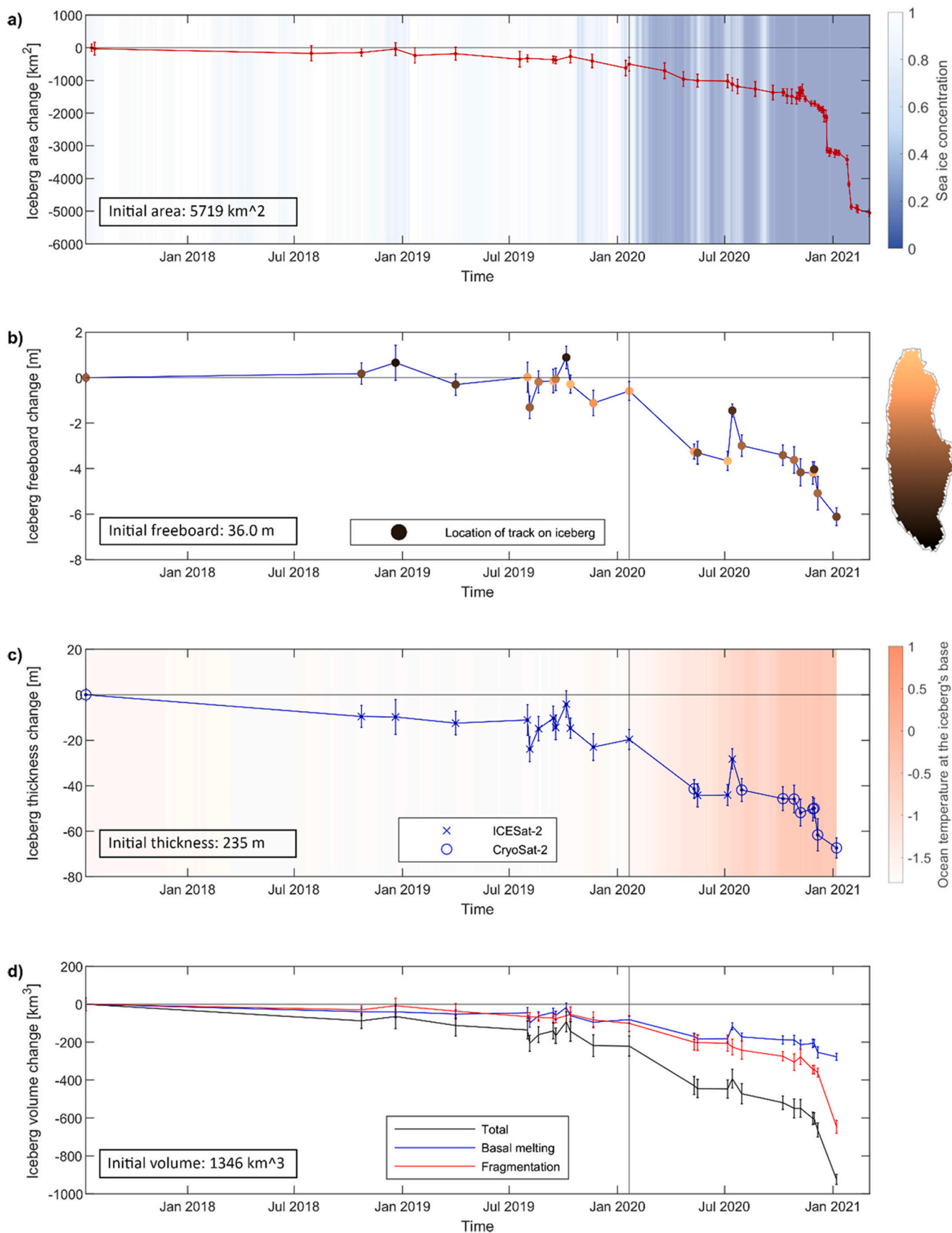
Fig. 6. Time series of changes in the A68A iceberg area (a), freeboard (b), thickness (c) and volume (d). The vertical line marks 21 January 2020, when the iceberg moved from the Weddell to the Scotia Sea (see Fig. 1). In panel (a) the background shading indicates sea ice concentration around the iceberg (OSI SAF, 2021) and in panel (c) the background shading indicates ocean temperature at the iceberg's base (Boyer et al., 2018).

Table 1

Annual change in the A68A iceberg area, thickness and volume in different regions along its trajectory.

Annual loss rate	Weddell Sea	Scotia Sea	Scotia Sea South	Scotia Sea North
Area [km^2/year]	−200 ± 82	−2807 ± 199	−1205 ± 286	−7400 ± 298
Thickness [m/year]	−7.8 ± 2.1	−49.5 ± 6.5	−36.4 ± 9.5	−86.9 ± 27.4
Volume [km^3/year]	−87.3 ± 21.0	−729.4 ± 50.4	−418.3 ± 75.7	−1621.7 ± 116.0
..through fragmentation	−44.7 ± 18.5	−538.3 ± 47.0	−244.1 ± 59.2	−1323.0 ± 90.9
..through melting	−42.6 ± 11.3	−191.2 ± 25.9	−174.2 ± 46.0	−298.7 ± 94.5

found a decrease of ~210 km², which is close to our estimate of 236 km² over a similar period (22 July 2017 to 22 January 2019). Scambos et al. (2008) identified three types of breakup for the A22A iceberg, which took a similar path: rift calvings, edge wastings and rapid disintegration. The breakups of A68B and A68C were probably rift calvings along pre-existing fractures; the breakup of numerous children icebergs in the last few months of our survey were rapid disintegration likely caused by surface melting, and edge-wasting and side-melting are likely the reason for the remaining area reductions (Fig. 6a).

Previous studies have also reported similar rates of iceberg freeboard and thickness change. Scambos et al. (2008) recorded no change in freeboard (0 ± 1.3 m) for the A22A iceberg over 17 months until it reached the tip of the Antarctic Peninsula and a reduction by 11.7 ± 2.3 m/year during its passage to South Georgia; we find similar rates for A68A of 0.2 ± 0.1 m/year and 5.7 ± 0.4 m/year in the same locations. This comparison also shows that our colocation improves the melt rate accuracy with respect to using tracks that only sample similar parts of the iceberg. Han et al. (2019) estimated the rate of thickness change of A68A to be 12.89 ± 3.34 m/year between February and November 2018 at sparse crossing points of CryoSat-2 ground tracks. Although we do not have measurements for the same period, interpolation of our colocated estimates suggests a value of 7.0 ± 0.8 m which is in reasonable agreement. In the Weddell Sea, Jansen et al. (2007) report melt rates in the range 0 to 12 m per year for the A38B iceberg, in good agreement with our estimate of 7.8 ± 2.1 m/year for A68A. Iceberg melting increases significantly in the Scotia Sea, and our estimate of 49.5 ± 6.5 m/year for A68A is almost identical to the value of ~48 m/year found by Jansen et al. (2007) for A38B. Bouhier et al. (2018) recorded melt rates for the B17A iceberg of 68.4 m/year in Scotia Sea South and 180 m/year in the Scotia Sea North. These values are approximately double the melt rates we have calculated for A68A in the same location (Table 1). A possible explanation could be that B17A started out with significantly higher freeboard of around 50 m, which means that its draft was exposed to ocean currents at a greater depth, where the water temperature is higher (Boyer et al., 2018). Concerning the contributions of melting and breakage, Tournadre et al. (2015) found that melting contributes only 18% over the whole life cycle of all large Antarctic icebergs – which is a slightly lower estimate than the 32% which we find for A68A during our study period. However, previous studies (Bouhier et al., 2018; Scambos et al., 2008) found that fragmentation becomes the dominant factor towards the end, which is also apparent from our data (Fig. 6d, Table 1), and calculating volume loss until e.g. March 2021 (when our area change time series ends) would have likely increased the share of fragmentation.

The very distinct melt rates in the Weddell and Scotia Sea can be explained by the different environmental conditions: First of all, icebergs experience significantly higher water and air temperatures in the Scotia Sea compared to the Weddell Sea (Scambos et al., 2008; see also Fig. 6c). Secondly, icebergs drifting freely in the Scotia Sea (Schodlok et al., 2006) are no longer sheltered by sea ice (Fig. 6a), exposing them

to wave erosion at the sides, forming a subsurface 'foot', which leads to calving owing to buoyancy stress (the so-called 'footloose mechanism'; Wagner et al., 2014). Apart from wave erosion at the waterline, ocean swell also induces strain on the iceberg, which can lead to crevasse and rift propagation (Li et al., 2018). Our observation that the initially southern part of the iceberg seems more stable (Fig. 6b) could be explained by the fact that this part is thinner (Figs. 2a and 5a) and therefore comes into contact with ocean water of a different temperature or current speed, as these are the two main drivers of iceberg melting (Bigg et al., 1997). In principle the iceberg could also have tilted to adjust its balance after break-offs from the northern part. Interestingly, we observe a notable thickness change in the Weddell Sea, although hardly any freeboard change was observed. This is because freeboard loss associated with basal melting and freeboard gain due to snow accumulation even out and hence a slow basal melting process can only be observed, when a snow layer is included in the calculations (Braakmann-Folgmann et al., 2021).

To constrain the intrusion of fresh water and nutrients, it is essential to determine where and by how much icebergs are melting (Silva et al., 2006). While volume loss due to basal melting serves as a lower bound estimate of freshwater and nutrient input, some of the area loss due to sidewall melting and edge-wastings also contribute, but are difficult to quantify in satellite observations. Children icebergs and larger edge-wastings, which form in larger calving events, travel further and take more time to melt (Tournadre et al., 2016). How quickly these melt depends on their size and the surrounding ocean conditions (Rackow et al., 2017; Stern et al., 2016); along the A68A trajectory, for example, melt rates vary from 10 to 100 m/year (Table 1) and ocean temperature at the iceberg's base increases from −1.8 °C to just over +1 °C (Fig. 6c). Children icebergs of sufficient length will also fragment further (England et al., 2020). And unlike large tabular icebergs, smaller icebergs with lengths similar to their thickness frequently roll over (Hamley and Budd, 1986). To track the entire freshwater and nutrient input, the trajectories and melting of all fragmented pieces would have to be considered. Furthermore, the amount of bioavailable iron and nutrients delivered by icebergs also depends on the amount of sediments contained in the iceberg (Raiswell et al., 2016).

Despite these unknowns, our observations allow for an initial assessment of A68A's impact on the ecosystem around South Georgia through scouring, melting and blockage. The closest recorded distance to the island was 62 km on 15 December 2020 with a mean draft of 141 ± 11 m. Seafloor bathymetry reveals a couple of shallower features within a distance of 52–65 km to the southern coastline (Fig. 1), where the iceberg could have grounded and where other icebergs may do so in future. Although A68A did not ground, it likely hit one of these features while turning (Fig. 1b). The shallowest bathymetry beneath the iceberg locations captured in satellite imagery is 150 m (Hogg et al., 2016). Although any scouring on the sea bed destroys the local benthic fauna (Barnes, 2017; Gutt, 2001), A68A's turn will have affected only a small area. As it fragmented into smaller pieces, the risk of blockage to foraging grounds (Kooyman et al., 2007) for the millions of penguins and seals, raising their offspring on South Georgia (Clarke et al., 2012; Joiris et al., 2015), was largely averted. For future icebergs, this scenario is most likely at the western tip of the island, where icebergs of similar draft can approach up to a few kilometers. However, birds, seals and whales that regularly feed in the highly productive waters surrounding South Georgia (Atkinson et al., 2001; Joiris et al., 2015) could also be influenced by the large amount of melt water and nutrients released by icebergs as they drift near to the island, altering the ocean properties and plankton occurrence (Arrigo et al., 2002; Smith et al., 2013; Vernet et al., 2012). Overall, A68A spent at least 96 days (28 November 2020 to 4 March 2021, when our observations end) within 300 km off the coastline. Assuming its children icebergs melted at the same rate of 0.43 ± 0.17 m per day, we estimate that 152 ± 61 Gt of fresh water mixed with nutrients was released during this time. More research should be conducted to study the impact of this alteration on the marine life

around South Georgia. As this is a common iceberg trajectory, our results could also help to predict the disintegration of other large tabular icebergs and to include their impact in ocean models (England et al., 2020; Martin and Adcroft, 2010; Rackow et al., 2017).

5. Conclusions

We have characterized the evolution of the A68A iceberg from its calving off the Larsen-C Ice Shelf in July 2017 to its disintegration close to South Georgia in early-2021. Although the iceberg was tabular, it had significant undulations in topography across its surface. Thus, accurate colocation of the iceberg's orientation is required to derive reliable estimates of its freeboard and thickness change over time from satellite altimetry. We estimate that the average iceberg thickness reduced from 235 ± 9 m at calving to 168 ± 10 m near South Georgia. Combined with observations of its area change determined from satellite imagery, we estimate an initial volume of 1346 ± 53 km^3 and 802 ± 34 Gt of ice loss from the main iceberg in 3.5 years. Around one third (254 ± 17 Gt) of the mass loss was through basal melting, which provides a lower bound estimate of the direct freshwater input along the iceberg's trajectory. Losses due to side melting and break-offs of smaller pieces will add to the immediate freshwater flux, and larger children icebergs will also contribute as they melt. Near South Georgia we estimate a fresh water input of 152 ± 61 Gt over ~3 months, potentially impacting the island's rich ecosystem. We confirm that the distinct environmental conditions in the Weddell and Scotia Sea lead to rapidly increasing rates of melting and fragmentation once icebergs travel north of the Antarctic Peninsula. Our detailed maps of the A68A iceberg thickness change (Braakmann-Folgmann et al., 2022) will be useful for investigations of the impact of this calving event on the stability of the Larsen-C Ice Shelf, and for more detailed studies on the effects of meltwater and nutrients released in the vicinity of South Georgia. As this is a common iceberg trajectory, our results could also help to model the disintegration of other large tabular icebergs that take a similar path and to include their impact in ocean models.

Supplementary data to this article can be found online at https://doi.org/10.1016/j.rse.2021.112855.

Data availability

All data used in this study are freely available: The iceberg trajectories are available from https://www.scp.byu.edu/data/iceberg/, CryoSat-2 data from https://science-pds.cryosat.esa.int/, ICESat-2 data from https://openaltimetry.org/data/icesat2/ and https://nsidc.org/data/atl03, Sentinel-1 data from https://scihub.copernicus.eu/dhus/ or https://www.polarview.aq/antarctic, Sentinel-3 data from https://apps.sentinel-hub.com/eo-browser, MODIS data from https://wvs.earthdata.nasa.gov/, the ERA-5 data from https://cds.climate.copernicus.eu/cdsapp#!/dataset/reanalysis-era5-single-levels, sea ice concentration data from ftp://osisaf.met.no/archive/ice/conc_amsr and ocean temperature from https://www.ncei.noaa.gov/data/oceans/woa/WOA18/DATA/temperature/. The daily maps of iceberg thickness are available from Mendeley Data (Braakmann-Folgmann et al., 2022).

Declaration of Competing Interest

The authors declare no conflict of interest.

Acknowledgments

References

Arrigo, K.R., Van Dijken, G.L., Ainley, D.G., Fahnestock, M.A., Markus, T., 2002. Ecological impact of a large Antarctic iceberg. Geophys. Res. Lett. 29 https://doi.org/10.1029/2001GL014160, 8-1-8–4.

Atkinson, A., Whitehouse, M.J., Priddle, J., Cripps, G.C., Ward, P., Brandon, M.A., 2001. South Georgia, Antarctica: a productive, cold water, pelagic ecosystem. Mar. Ecol. Prog. Ser. 216, 279–308. https://doi.org/10.3354/meps216279.

Barnes, D.K.A., 2017. Iceberg killing fields limit huge potential for benthic blue carbon in Antarctic shallows. Glob. Chang. Biol. 23, 2649–2659. https://doi.org/10.1111/gcb.13523.

Biddle, L.C., Kaiser, J., Heywood, K.J., Thompson, A.F., Jenkins, A., 2015. Ocean glider observations of iceberg-enhanced biological production in the northwestern Weddell Sea. Geophys. Res. Lett. 42, 459–465. https://doi.org/10.1002/2014GL062850.

Bigg, G.R., Wadley, M.R., Stevens, D.P., Johnson, J.A., 1997. Modelling the dynamics and thermodynamics of icebergs. Cold Reg. Sci. Technol. 26, 113–135. https://doi.org/10.1016/S0165-232X(97)00012-8.

Bintanja, R., Van Oldenborgh, G.J., Katsman, C.A., 2015. The effect of increased fresh water from Antarctic ice shelves on future trends in Antarctic sea ice. Ann. Glaciol. 56, 120–126. https://doi.org/10.3189/2015AoG69A001.

Bouhier, N., Tournadre, J., Rémy, F., Gourves-Cousin, R., 2018. Melting and fragmentation laws from the evolution of two large Southern Ocean icebergs estimated from satellite data. Cryosphere 12, 2267–2285. https://doi.org/10.5194/tc-12-2267-2018.

Boyer, T.P., Garcia, Locarnini, Hernan E., Zweng, Ricardo A., Mishonov, Melissa M., Reagan, Alexey V., Weathers, James R., Baranova, Katharine A., Olga, K., Seidov, D., Smolyar, I.V., 2018. World Ocean Atlas 2018.

Braakmann-Folgmann, A., Shepherd, A., Ridout, A., 2021. Changes in the area, thickness, and volume of the Thwaites 'B30' iceberg observed by satellite altimetry and imagery. Cryosphere Discuss. 1–27.

Braakmann-Folgmann, A., Shepherd, A., Gerrish, L., Izzard, J., Ridout, A., 2022. A68A Iceberg Thickness Maps (Jul 2017-Jan 2021). https://doi.org/10.17632/26dg4fwkhb.1.

Budge, J.S., Long, D.G., 2018. A comprehensive database for Antarctic iceberg tracking using scatterometer data. IEEE J. Sel. Top. Appl. Earth Obs. Remote Sens. 11, 434–442. https://doi.org/10.1109/JSTARS.2017.2784186.

Clarke, A., Croxall, J.P., Poncet, S., Martin, A.R., Burton, R., 2012. Important bird areas: South Georgia. Br. Bird 105, 118–144.

Copernicus Climate Change Service, 2018. ERA5 Hourly Data on Single Levels from 1979 to Present. https://doi.org/10.24381/cds.adbb2d47.

Dryak, M.C., Enderlin, E.M., 2020. Analysis of Antarctic Peninsula glacier frontal ablation rates with respect to iceberg melt-inferred variability in ocean conditions. J. Glaciol. 66, 457–470. https://doi.org/10.1017/jog.2020.21.

Duprat, L.P.A.M., Bigg, G.R., Wilton, D.J., 2016. Enhanced Southern Ocean marine productivity due to fertilization by giant icebergs. Nat. Geosci. 9, 219–221. https://doi.org/10.1038/ngeo2633.

England, M.R., Wagner, T.J.W., Eisenman, I., 2020. Modeling the breakup of tabular icebergs. Sci. Adv. 6, 1–9. https://doi.org/10.1126/sciadv.abd1273.

Fichefet, T., Morales Maqueda, M.A., 1999. Modelling the influence of snow accumulation and snow-ice formation on the seasonal cycle of the Antarctic sea-ice cover. Clim. Dyn. 15, 251–268. https://doi.org/10.1007/s003820050280.

GEBCO Compilation Group, 2019. GEBCO 2019 Grid. https://doi.org/10.5285/836f016a-33be-6ddc-e053-6c86abc0788e.

Greene, C.A., Gwyther, D.E., Blankenship, D.D., 2017. Antarctic mapping tools for MATLAB. Comput. Geosci. 104, 151–157. https://doi.org/10.1016/j.cageo.2016.08.003.

Grimm, I., 2021. Assessing Effects of Iceberg A-68a on the Weddell Sea and South Georgia Ecosystems.

Grosfeld, K., Schröder, M., Fahrbach, E., Gerdes, R., Mackensen, A., 2001. How iceberg calving and grounding change the circulation and hydrography in the Filchner Ice Shelf–Ocean System. J. Geophys. Res. 106, 9039–9055.

Gutt, J., 2001. On the direct impact of ice on marine benthic communities, a review. Polar Biol. 24, 553–564. https://doi.org/10.1007/s003000100262.

Hamley, T.C., Budd, W.F., 1986. Antarctic iceberg distribution and dissolution. J. Glaciol. 32, 242–251. https://doi.org/10.1017/s0022143000015574.

Han, H., Lee, S., Kim, J.I., Kim, S.H., Kim, H.C., 2019. Changes in a giant iceberg created from the collapse of the Larsen C ice shelf, Antarctic Peninsula, derived from Sentinel-1 and CryoSat-2 data. Remote Sens. 11, 1–14. https://doi.org/10.3390/rs11040404.

Helly, J.J., Kaufmann, R.S., Stephenson, G.R., Vernet, M., 2011. Cooling, dilution and mixing of ocean water by free-drifting icebergs in the Weddell Sea. Deep. Res. Part II Top. Stud. Oceanogr. 58, 1346–1363. https://doi.org/10.1016/j.dsr2.2010.11.010.

Hogg, A.E., Gudmundsson, G.H., 2017. Commentary: impacts of the Larsen-C ice shelf calving event. Nat. Clim. Chang. 7, 540–542. https://doi.org/10.1038/nclimate3359.

Hogg, O., Huvenne, V.A., Griffiths, H.J., Dorschel, B., Linse, K., 2016. A Bathymetric Compilation of South Georgia, 1985–2015. https://doi.org/10.5285/ce8bf6be-4b5f-454c-9165-73ab4c3baf23.

Holland, P.R., Corr, H.F.J., Vaughan, D.G., Jenkins, A., Skvarca, P., 2009. Marine ice in Larsen ice shelf. Geophys. Res. Lett. 36, 1–6. https://doi.org/10.1029/2009GL038162.

Holland, P.R., Corr, H.F.J., Pritchard, H.D., Vaughan, D.G., Arthern, R.J., Jenkins, A., Tedesco, M., 2011. The air content of Larsen ice shelf. Geophys. Res. Lett. 38, 1–6. https://doi.org/10.1029/2011GL047245.

International Organization for Standardization, 1998. ISO 4355 Bases for Design on Structures – Determination of Snow Loads on Roofs.

Jansen, D., Schodlok, M., Rack, W., 2007. Basal melting of A-38B: a physical model constrained by satellite observations. Remote Sens. Environ. 111, 195–203. https://doi.org/10.1016/j.rse.2007.03.022.

Jansen, D., Luckman, A., Kulessa, B., Holland, P.R., King, E.C., 2013. Marine ice formation in a suture zone on the Larsen C ice shelf and its influence on ice shelf dynamics. J. Geophys. Res. Earth Surf. 118, 1628–1640. https://doi.org/10.1002/jgrf.20120.

Jansen, D., Luckman, A., Cook, A., Bevan, S., Kulessa, B., Hubbard, B., Holland, P.R., 2015. Brief communication: newly developing rift in Larsen C ice shelf presents significant risk to stability. Cryosphere 9, 1223–1227. https://doi.org/10.5194/tc-9-1223-2015.

Jenkins, A., 1999. The impact of melting ice on ocean waters. J. Phys. Oceanogr. 29, 2370–2381. https://doi.org/10.1175/1520-0485(1999)029<2370:TIOMIO>2.0.CO;2.

Joiris, C.R., Humphries, G.R.W., D'Hert, D., Robert, H., Beudels-Jamar, R.C., 2015. Major hotspots detected along the Scotia Ridge in autumn for southern right whales Eubalaena australis, Antarctic fur seals Arctocephalus gazella and Antarctic prions Pachyptila desolata. Adv. Polar Sci. 26, 282–291. https://doi.org/10.13679/j.advps.2015.4.00282.

Kooyman, G.L., Ainley, D.G., Ballard, G., Ponganis, P.J., 2007. Effects of giant icebergs on two emperor penguin colonies in the Ross Sea, Antarctica. Antarct. Sci. 19, 31–38. https://doi.org/10.1017/S0954102007000065.

Kurtz, N.T., Markus, T., 2012. Satellite observations of Antarctic sea ice thickness and volume. J. Geophys. Res. Ocean 117, 1–9. https://doi.org/10.1029/2012JC008141.

Kwok, R., Cunningham, G.F., 2008. ICESat over Arctic sea ice: estimation of snow depth and ice thickness. J. Geophys. Res. Ocean 113, 1–17. https://doi.org/10.1029/2008JC004753.

Li, Tian, Shokr, M., Liu, Y., Cheng, X., Li, Teng, Wang, F., Hui, F., 2018. Monitoring the tabular icebergs C28A and C28B calved from the Mertz Ice Tongue using radar remote sensing data. Remote Sens. Environ. 216, 615–625. https://doi.org/10.1016/j.rse.2018.07.028.

Ligtenberg, S.R.M., Helsen, M.M., Van Den Broeke, M.R., 2011. An improved semi-empirical model for the densification of Antarctic firn. Cryosphere 5, 809–819. https://doi.org/10.5194/tc-5-809-2011.

Lopez-Lopez, L., Parmiggiani, F., Moctezuma-Flores, M., Guerrieri, L., 2021. On the detection and long-term path visualisation of a-68 iceberg. Remote Sens. 13, 1–13. https://doi.org/10.3390/rs13030460.

Martin, T., Adcroft, A., 2010. Parameterizing the fresh-water flux from land ice to ocean with interactive icebergs in a coupled climate model. Ocean Model 34, 111–124. https://doi.org/10.1016/j.ocemod.2010.05.001.

Merino, N., Le Sommer, J., Durand, G., Jourdain, N.C., Madec, G., Mathiot, P., Tournadre, J., 2016. Antarctic icebergs melt over the Southern Ocean : climatology and impact on sea ice. Ocean Model 104, 99–110. https://doi.org/10.1016/j.ocemod.2016.05.001.

Mouginot, J., Rignot, E., Scheuchl, B., 2019. Continent-Wide, Interferometric SAR Phase, Mapping of Antarctic Ice Velocity. Geophys. Res. Lett. 46, 9710–9718. https://doi.org/10.1029/2019GL083826.

OSI SAF, 2021. AMSR-2 Sea Ice Concentration Product of the EUMETSAT Ocean and Sea Ice Satellite Application Facility.

Rackow, T., Wesche, C., Timmermann, R., Hellmer, H.H., Juricke, S., Jung, T., 2017. A simulation of small to giant Antarctic iceberg evolution: differential impact on climatology estimates. J. Geophys. Res. Ocean 3170–3190. https://doi.org/10.1002/2016JC012513.Received.

Raiswell, R., Hawkings, J.R., Benning, L.G., Baker, A.R., Death, R., Albani, S., Mahowald, N., Krom, M.D., Poulton, S.W., Wadham, J., Tranter, M., 2016. Potentially bioavailable iron delivery by iceberg-hosted sediments and atmospheric dust to the polar oceans. Biogeosciences 13, 3887–3900. https://doi.org/10.5194/bg-13-3887-2016.

Rignot, E., Casassa, G., Gogineni, P., Krabill, W., Rivera, A., Thomas, R., 2004. Accelerated ice discharge from the Antarctic Peninsula following the collapse of Larsen B ice shelf. Geophys. Res. Lett. 31, 2–5. https://doi.org/10.1029/2004GL020697.

Rott, H., Skvarca, P., Nagler, T., 1996. Rapid collapse of northern Larsen ice shelf, Antarctica. Science 80 (271), 788–792. https://doi.org/10.1126/science.271.5250.788.

Scambos, T., Ross, R., Bauer, R., Yermolin, Y., Skvarca, P., Long, D., Bohlander, J., Haran, T., 2008. Calving and ice-shelf break-up processes investigated by proxy: Antarctic tabular iceberg evolution during northward drift. J. Glaciol. 54, 579–591. https://doi.org/10.3189/002214308786570836.

Schodlok, M.P., Hellmer, H.H., Rohardt, G., Fahrbach, E., 2006. Weddell Sea iceberg drift: five years of observations. J. Geophys. Res. Ocean 111, 1–14. https://doi.org/10.1029/2004JC002661.

Shepherd, A., Gilbert, L., Muir, A.S., Konrad, H., McMillan, M., Slater, T., Briggs, K.H., Sundal, A.V., Hogg, A.E., Engdahl, M.E., 2019. Trends in Antarctic ice sheet elevation and mass. Geophys. Res. Lett. 46, 8174–8183. https://doi.org/10.1029/2019GL082182.

Silva, T.A.M., Bigg, G.R., Nicholls, K.W., 2006. Contribution of giant icebergs to the Southern Ocean freshwater flux. J. Geophys. Res. 111, 1–8. https://doi.org/10.1029/2004JC002843.

Smith, K.L., Robison, B.H., Helly, J.J., Kaufmann, R.S., Ruhl, H.A., Shaw, T.J., Twining, B.S., Vernet, M., 2007. Free-drifting icebergs: hot spots of chemical and biological enrichment in the Weddell Sea. Science 80 (317), 478–482. https://doi.org/10.1126/science.1142834.

Smith, K.L., Sherman, A.D., Shaw, T.J., Sprintall, J., 2013. Icebergs as unique lagrangian ecosystems in polar seas. Annu. Rev. Mar. Sci. 5, 269–287. https://doi.org/10.1146/annurev-marine-121211-172317.

Stern, A.A., Adcroft, A., Sergienko, O., 2016. The effects of Antarctic iceberg calving-size distribution in a gloabl climate model. J. Geophys. Res. Ocean 1–14. https://doi.org/10.1002/2016JC011835.Received.

Storto, A., Oddo, P., Cozzani, E., Coelho, E.F., 2019. Introducing along-track error correlations for altimetry data in a regional ocean prediction system. J. Atmos. Ocean. Technol. 36, 1657–1674. https://doi.org/10.1175/JTECH-D-18-0213.1.

Tilling, R.L., Ridout, A., Shepherd, A., 2018. Estimating Arctic sea ice thickness and volume using CryoSat-2 radar altimeter data. Adv. Sp. Res. 62, 1203–1225. https://doi.org/10.1016/j.asr.2017.10.051.

Tournadre, J., Bouhier, N., Girard-Ardhuin, F., Remy, F., 2015. Large icebergs characteristics from altimeter waveforms analysis. J. Geophys. Res. Ocean 120, 2121–2128. https://doi.org/10.1002/2014JC010502.

Tournadre, J., Bouhier, N., Girard-Ardhuin, F., Rémy, F., 2016. Antarctic icebergs distributions 1992–2014. J. Geophys. Res. Ocean 121, 327–349. https://doi.org/10.1002/2015JC011178.

Vernet, M., Smith, K.L., Cefarelli, A.O., Helly, J.J., Kaufmann, R.S., Lin, H., Long, D.G., Murray, A.E., Robison, B.H., Ruhl, H.A., Shaw, T.J., Sherman, A.D., Sprintall, J., Stephenson, G.R., Stuart, K.M., Twining, B.S., 2012. Islands of ice: influence of free-drifting Antarctic icebergs on pelagic marine ecosystems. Oceanography 25, 38–39. https://doi.org/10.5670/oceanog.2012.72.

Wagner, T.J.W., Wadhams, P., Bates, R., Elosegui, P., Stern, A., Vella, D., Abrahamsen, E.P., Crawford, A., Nicholls, K.W., 2014. The "footloose" mechanism: iceberg decay from hydrostatic stresses. Geophys. Res. Lett. 41, 5522–5529. https://doi.org/10.1002/2014GL060832.

Wise, M.G., Dowdeswell, J.A., Jakobsson, M., Larter, R.D., 2017. Evidence of marine ice-cliff instability in Pine Island Bay from iceberg-keel plough marks. Nature 550, 506–510. https://doi.org/10.1038/nature24458.

Wu, S.Y., Hou, S., 2017. Impact of icebergs on net primary productivity in the Southern Ocean. Cryosphere 11, 707–722. https://doi.org/10.5194/tc-11-707-2017.